

Direct X-Ray Detection of the Spin Hall Effect in CuBi

Sandra Ruiz-Gómez^{1,2,*}, Rubén Guerrero,³ Muhammad W. Khaliq², Claudia Fernández-González,^{1,3}
 Jordi Prat,² Andrés Valera³, Simone Finizio,⁴ Paolo Perna,³ Julio Camarero,^{3,5} Lucas Pérez^{1,3,6},
 Lucía Aballe² and Michael Foerster²

¹*Departamento de Física de Materiales, Universidad Complutense de Madrid, Plaza de las Ciencias 1, 28040 Madrid, Spain*


²*ALBA Synchrotron Light Facility, CELLS, Carrer de la Llum, 2-26, E-08290 Bellaterra, Spain*

³*Instituto Madrileño de Estudios Avanzados, IMDEA Nanociencia, Calle Faraday 9, 28049 Madrid, Spain*

⁴*Swiss Light Source, Paul Scherrer Institut, CH-5232 Villigen PSI, Switzerland*

⁵*Departamento de Física de la Materia Condensada e Instituto “Nicolás Cabrera” and Condensed Matter Physics Center (IFIMAC), Universidad Autónoma de Madrid (UAM), Campus de Cantoblanco. Madrid 28049, Spain*

⁶*Surface Science and Magnetism of Low Dimensional Systems, UCM, Unidad Asociada al CSIC (IQFR), 28040 Madrid, Spain*

 (Received 5 July 2021; revised 11 February 2022; accepted 12 July 2022; published 1 September 2022)

The spin Hall effect and the inverse spin Hall effect are important spin-charge conversion mechanisms. The direct spin Hall effect induces a surface spin accumulation from a transverse charge current due to spin-orbit coupling even in nonmagnetic conductors. However, most detection schemes involve additional interfaces, leading to large scattering in reported data. Here we perform interface-free x-ray spectroscopy measurements at the Cu $L_{3,2}$ absorption edges of highly Bi-doped Cu ($\text{Cu}_{95}\text{Bi}_5$). The detected x-ray magnetic circular dichroism signal corresponds to an induced magnetic moment of $(2.2 \pm 0.5) \times 10^{-12} \mu_B \text{ \AA}^{-1} \text{ cm}^2$ per Cu atom averaged over the probing depth, which is of the same order of magnitude as found for Pt measured by magneto-optics. The results highlight the importance of interface-free measurements to assess material parameters and the potential of CuBi for spin-charge conversion applications.

DOI: 10.1103/PhysRevX.12.031032

Subject Areas: Condensed Matter Physics, Spintronics

I. INTRODUCTION

Since the discovery of the giant magnetoresistance effect triggered the field of spintronics, spin-dependent electron transport phenomena have been widely investigated and have gained importance in research and technological applications. Within spintronics, the spin Hall effect (SHE) may be considered a more recent discovery [1], although it was predicted several decades ago (Dyakonov and Perel [2], based on Mott scattering [3]). The SHE and its inverse refer to orthogonal charge and spin currents which can arise through different mechanisms, but always due to spin-orbit coupling. For comprehensive reviews, refer to Refs. [4,5]. The SHE is already widely used to generate and detect spin currents. It can drive magnetic excitations more efficiently than spin transfer torque, for

instance, in spin-orbit torque magnetic random access memory. The direct SHE generates a pure spin current in a nonmagnetic conductor, perpendicular to the electron flow, with the spin polarization perpendicular to both the spin current and the electron current. The ratio of spin and charge current is the spin Hall angle (SHA), $\alpha = (\sigma_{xy}^s / \sigma_{xx}^c)(e/\hbar)$ [5], where σ_{xy}^s and σ_{xx}^c are the spin and charge current conductivities, respectively. The SHA measures the efficiency of charge to spin conversion and is thus the main figure of merit for applications. The spin current results in a spin accumulation at the edges of the conductor, on the length scale of the spin diffusion length [see schematic in Fig. 1(a)].

First observations of the SHE in semiconductors used optical detection [6,7], but optical methods have proven challenging for metallic systems, due to their considerably shorter spin diffusion lengths, an achievement only recently realized for Pt and W by Stamm and co-workers [8]. In metals, electrical detection schemes like nonlocal spin valves, inverse spin Hall effect, spin Seebeck effect, spin-orbit torque, etc. are typically used. However, all those techniques involve an interface with another magnetic material and, as a consequence, the combined materials' and interface properties are measured, which might include

*Present address: Max Planck Institute for Chemical Physics of Solids, Dresden 01187, Germany.

Published by the American Physical Society under the terms of the Creative Commons Attribution 4.0 International license. Further distribution of this work must maintain attribution to the author(s) and the published article's title, journal citation, and DOI.

other sources of spin-orbit interactions such as the Rashba effect. Possibly this is one of the reasons for the variability of reported results for the spin Hall angle and diffusion length or lifetime in metals. The large scattering of reported results from these methods for the same material and temperature (e.g., see Table III of Ref. [4]) call for a more direct and interface-free approach.

X-ray spectroscopy and x-ray magnetic circular dichroism (XMCD) have become reference tools for precision measurements of small or diluted magnetic signals [9–13]. X-ray detection of the SHE is highly desirable since it gives element specific access to the electronic information and can provide a clear spectroscopic fingerprint. Furthermore, performing the measurement on a single layer can eliminate the influence of an interface. Still using heterostructures, Stamm *et al.* [14] investigated with XMCD spectroscopy Pt/Co and Pt/*NM* (*NM* = Ti, Cr, Cu) bilayers for a spin accumulation in the overlayer due to the SHE in Pt. While a clear change in the Co moment was observed, no signal above noise limit was detected in the *NM* for the other cases. Since the expected spin accumulation in Pt should have been above the detection limit, the lack of a clear signal may again be due to the presence of the Pt/*NM* interface. Thus, to the best of our knowledge, the direct detection of spin accumulation due to the SHE by x-ray spectroscopic methods is still lacking.

As a general trend, heavy metals such as Pt, W, etc. with high spin-orbit coupling are expected to give rise to comparatively large spin Hall angles. Although Cu does not exhibit a high SHA, it has been experimentally demonstrated that by adding only 0.5% Bi doping, a giant SHA $\alpha_{\text{CuBi}} = -0.11$ (for the CuBi alloy and $\alpha_{\text{imp}} = -0.24$ for the skew scattering mechanism) [15] can be obtained, higher than the one of Pt, $\alpha_{\text{Pt}} = 0.068$ [16,17] ($\alpha_{\text{Pt}} = 0.08$ in Ref. [8]). More recently, thin Cu films with higher Bi doping levels, up to 10%, have been prepared, without signs of Bi segregation [18]. Interfaces of these films with yttrium iron garnet (YIG) exhibit a large spin mixing conductance $g_{\uparrow\downarrow}$ [19,20], i.e., transport efficiency of spin current, indicated by the increased damping in spin pumping ferromagnetic resonance measurements, yielding values $g_{\uparrow\downarrow}$ ($\text{Cu}_{96}\text{Bi}_4/\text{YIG}$) = $7 \times 10^{18} \text{ m}^{-2}$) [18] comparable to those of Pt/YIG [$g_{\uparrow\downarrow}(\text{Pt}/\text{YIG}) = 6.9$ to $9 \times 10^{18} \text{ m}^{-2}$] [19]. However, based on the work of Niimi *et al.* [15] for CuBi, one may have anticipated an even higher SHE in such highly Bi-doped Cu. This discrepancy could be related to the quality of the Pt/YIG and CuBi/YIG interfaces, highlighting again the need for a more direct method in order to assess the true material parameters.

CuBi is a good candidate for the x-ray detection of the SHE due to the convenient Cu $L_{3,2}$ absorption edge in the soft x-ray range. In fact, Kukreja *et al.* [21] reported soft x-ray spectroscopic measurements of a transient spin accumulation in Cu induced by a spin polarized current from an adjacent Co layer, proving that small spin

accumulations in Cu can indeed be measured with x rays. They identified a spectral feature of the spin accumulation at the rising edge of the L_3 absorption peak, corresponding to transitions to the Fermi level. In addition, a Cu XMCD signal induced by proximity to Co and enhanced by current injection was found close to the L_3 peak. More recently, using the same setup, Ding *et al.* have observed a spin accumulation in Cu induced by spin pumping from an adjacent $\text{Ni}_{80}\text{Fe}_{20}$ layer detected at the Cu L_3 edge [22].

Here we report the detection of spin accumulation under electric current flow, i.e., spin Hall effect, in the surface of highly Bi-doped $\text{Cu}_{95}\text{Bi}_5$ using soft x-ray photoemission electron microscopy (PEEM). The measurements at the $L_{3,2}$ absorption edges were performed on the top of single material CuBi electrodes on insulating SiO_x/Si substrates, i.e., free of any interface effect. The PEEM information depth is limited to about 5 nm by the electron escape length, allowing us to selectively detect the spin accumulation in the upper surface of the electrode (the sensitivity as function of depth z is approximately $e^{-z/2 \text{ nm}}$ [23]). In other words, the signals from the upper and lower surfaces do not compensate in PEEM as they would if the whole thickness was measured, e.g., in transmission geometry. This microscopy approach enables us to focus on small electrode structures and achieve high current densities at moderate total power dissipated. The sample geometry was chosen to compensate different backgrounds by the use of a symmetric electrode design (Fig. 1). This layout enables us to reduce the background variations, in particular, those associated with the voltage drop along the electrode due to the current and to the inhomogeneity of the x-ray illumination for opposite polarization. Thanks to these factors, we have been able to detect a clear dichroic (XMCD) signal of the x-ray absorption in CuBi associated to a SHE-induced surface spin accumulation.

II. EXPERIMENTAL

$\text{Cu}_{95}\text{Bi}_5$ thin films were deposited by coevaporation at room temperature onto Si substrates with a 200-nm-thick thermally grown oxide layer to avoid current shunting in the experiments. The electrode structures were patterned by electron beam lithography followed by lift-off (details in Appendix A). The preparation and characterization of highly Bi-doped Cu films have been described in Ref. [18]. The thickness of the CuBi electrodes was varied between 20 and 50 nm. After growth, samples were capped *in situ* with a 3 nm Al_2O_3 layer in order to avoid surface oxidation. This layer was removed by Ar^+ sputtering before measurements.

X-ray spectroscopic measurements were performed at the LEEM-PEEM (low-energy electron microscopy–photoemission electron microscopy) experimental station of the CIRCE beam line of the ALBA Synchrotron, which has excellent stability [24]. Samples were mounted onto printed circuit boards and contacted with wire bonds, using

dedicated sample holders [25]. Direct current (dc, 30–120 mA) was injected into the electrodes using a current source purposely designed for the PEEM instrument. A single dataset was obtained using pulsed current injection (millisecond range) to reduce heating and allow an even higher current density. During the measurements, the sample holder was cooled down to about 220 K. The dc currents of 30–120 mA injected into the samples resulted in a moderate increase of the pressure in the UHV chamber from Joule heating (reaching 10^{-9} mbar while starting in the 10^{-10} mbar range). When the current values were too high, we observed in real time the segregation of small clusters to the surface, which are rich in Bi (see Appendix B). All the data points used in this study were acquired below this current limit. In the PEEM instrument, the x-ray beam incidence onto the sample is 16° grazing, which results in a mixed sensitivity to in-plane and out-of-plane magnetic moments in XMCD measurements (with 0.96 and 0.28 efficiency, respectively). Therefore, by assuming a pure in-plane spin polarization in our

experiment, a correction factor of 1.04 is applied to the final extracted XMCD values. To obtain a single data point, i.e., an XMCD image at a fixed photon energy, we averaged a number of single images (typically 200) for each of the two circular polarizations [left- (*CP*) and right-handed (*CN*)], before calculating the pixelwise asymmetry $\text{XMCD} = \{I(\text{CP}) - I(\text{CN})\} / \{I(\text{CP}) + I(\text{CN})\}$, where $I(\text{CP/CN})$ denotes the count rate of the low-energy secondary electrons for a pixel in the image. The XMCD value for one part of the electrode is obtained as the average of all pixels in that area.

III. RESULTS AND DISCUSSION

The schematic of the experiment is shown in Fig. 1(a), where the circularly polarized x-ray beam illuminates the sample from the right (blue arrow). The yellow arrows mark the direction of the electron flow in the electrode loops, being opposite in Figs. 1(b) and 1(c). The current injection (current density $j = 1.7 \times 10^7 \text{ A cm}^{-2}$) gives rise

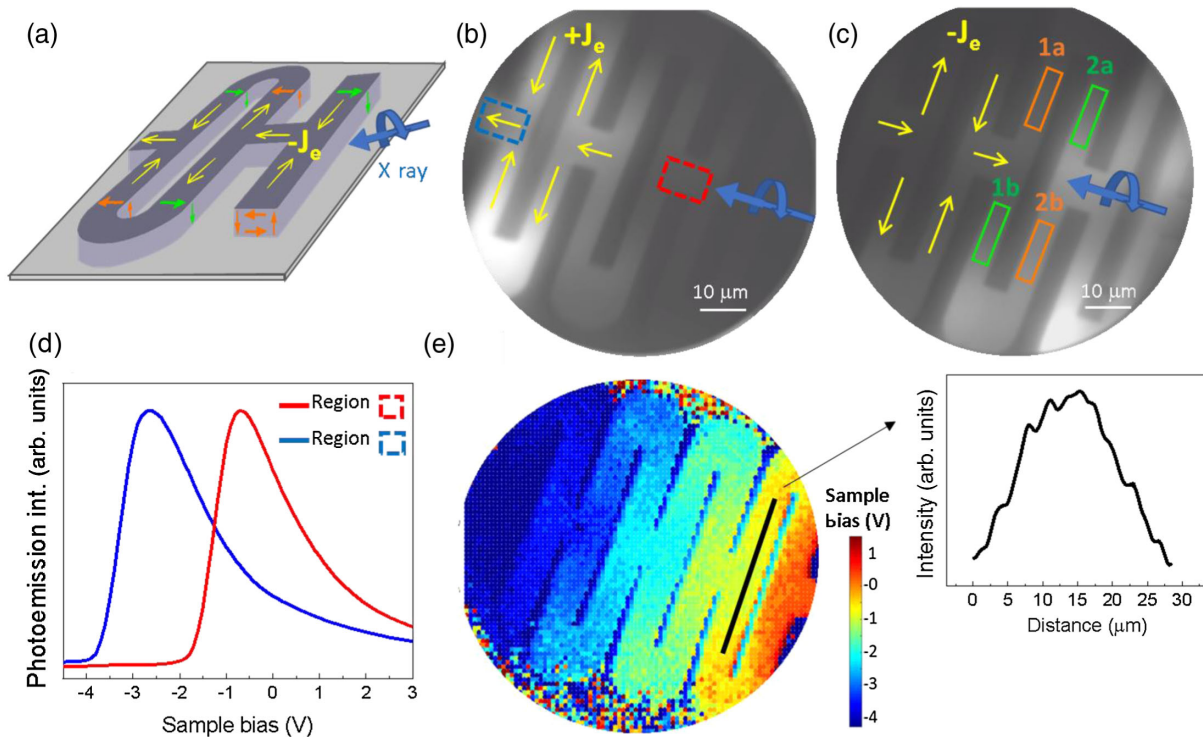


FIG. 1. Sample layout and effect of current injection. (a) Schematic of the experimental geometry, indicating the electron flow (yellow arrows), as well as the accumulated spin polarization at the different surfaces (green and orange arrows). The circularly polarized x-ray beam, shown in blue, impinges from the right under 16° grazing angle, providing sensitivity to the spin polarization in the beam direction. (b) PEEM image of a measured device during positive electron flow (negative current) (yellow arrows). The surface electric potential variation due to the driving voltage causes an intensity variation from left to right. Red and blue boxes show the areas corresponding to the spectra in (d). (c) PEEM image for negative electron flow. The associated potential drop is opposite to that in (b). The green and orange boxes in (c) indicate the two types of areas with the same current direction and thus spin accumulation. (d) Spectra of the photoemission intensity versus sample bias voltage for the blue and red boxes in (b). The different local potential is reflected in a shift of the low-energy secondary electron peak versus sample bias voltage. (e) Color map of the sample bias voltage value at which the maximum of photoemission intensity is located. The profile along the black line (inset) indicates that the current is correctly flowing through the electrodes.

to a voltage drop along the path of the electrons, which is detected in PEEM as a shift of the secondary electron spectrum with respect to the sample bias voltage (nominal photoelectron kinetic energy). In Fig. 1(d), we show two spectra obtained from the red and blue areas of Fig. 1(b), with a relative shift of about 2 V. The color map in Fig. 1(e) indicates at which bias voltage the spectra reached maximum intensity for a given area. The potential variation along the black line as shown in the inset in Fig. 1(e) demonstrates that the current is indeed following the electrode path. The potential variation along the electrode is reproduced by finite element simulations and indicates a resistivity of $13 \mu\Omega \text{ cm}$ of the patterned CuBi electrode at 220 K (see Appendix C). Images in Figs. 1(b) and 1(c) were taken at constant sample bias voltage and thus reflect the potential variation as intensity. The intensity variation will differ for opposite driving current, making a measurement scheme with alternating injected currents (or lock-in detection) impractical for PEEM. Therefore, the electrode layout was chosen to provide equipotential points in the middle, permitting the direct comparison of areas with the same electric potential but opposite current direction. Those areas are vertically aligned, for example, the orange and green boxes, labeled 1(a) and 1(b), in Fig. 1(c). Since the accumulated spin polarization is opposite in consecutive branches (e.g., 1 and 2), the dichroic component of the x-ray absorption, taken as 1/2 of the up-down asymmetry for each branch, alternates.

To characterize the $\text{Cu}_{95}\text{Bi}_5$ electrodes, we have performed x-ray photoelectron spectroscopy (XPS) and x-ray absorption spectroscopy (XAS). The protective Al capping layer was removed *in situ* by Ar ion sputtering before all measurements. The Bi 4*f* XPS shows mostly metallic Bi with a small oxide component [Fig. 2(a)]. In contrast, measurements of samples exposed to air after the capping removal showed almost fully oxidized Bi (Appendix D). XPS spectra are extremely surface sensitive, with a probing depth on the order of 1 nm. The XAS of the Cu $L_{3,2}$ edges indicates that the Cu in the electrode is also metallic [Fig. 2(b)]. Together with the spectrum, the extracted XMCD signal is plotted for different photon energies. Each single data point is the average of at least three independent measurements. The determination of this SHE signal, which is explained in detail in Appendix F, includes a parabolical fitting of the background to highlight the SHE contribution.

Figure 2(b) shows the XAS spectra together with the XMCD signal extracted at a selected number of photon energies in which the SHE contribution should be either negligible (for off-peak energies) or maximum and opposite (for L_3 and L_2 peak energies). As expected, the SHE-induced XMCD signal has a maximum at the L_3 edge and is inverted at the L_2 edge. However, even for off-peak energies, where no XMCD signal is expected, finite values are found (see also Fig. 10). This offset was found to be

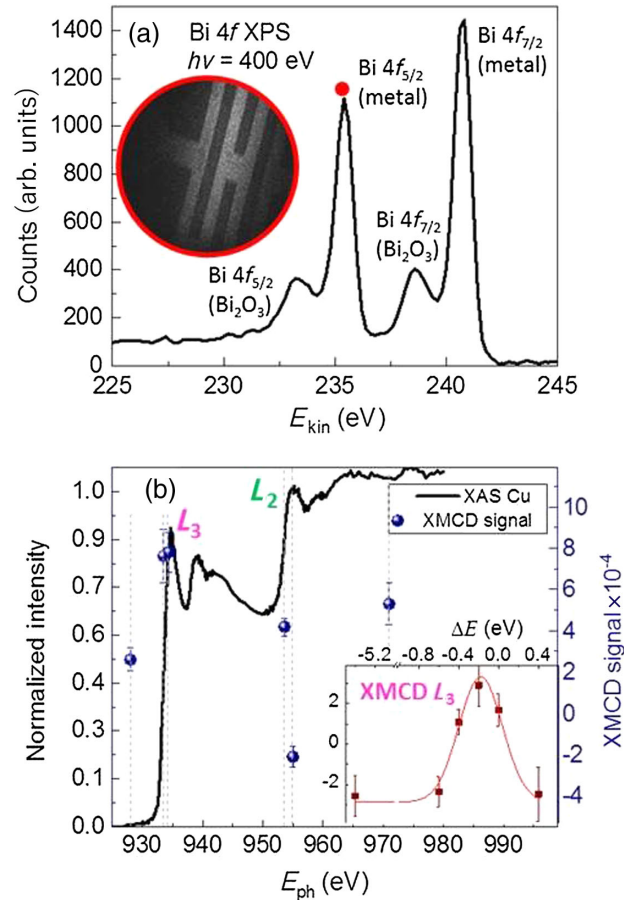


FIG. 2. X-ray spectroscopy of the CuBi electrodes and the spin accumulation signal measured in sample S1. (a) Photoelectron spectrum of the Bi 4*f* core level, showing a small surface oxide contribution. Inset: XPEEM image at the Bi 4*f*_{5/2} peak (marked with a red dot in the spectrum). Bismuth is homogeneously distributed in the electrode surface. (b) X-ray absorption spectrum of the Cu L edges together with one dataset of XMCD values. Inset: XMCD scan close to the L_3 edge for sample S4 (y axis shows the same units as the right-hand axis of the main panel).

inconsistent between different measurement series and thus we conclude that even after our best efforts, small background variations in the XMCD images are of the same order of magnitude as the SHE signal in our data. These variations most likely come from the different beam intensity distribution for opposite beam polarizations. However, for each single run at a fixed current value, after thermalization, the offset was roughly constant over time and photon energy, so that we can normalize the XMCD signal for the L_3 and L_2 peaks by subtracting the value obtained by an immediately preceding measurement at a prepeak photon energy. A similar offset (of opposite sign) is seen in the inset of Fig. 2(b) where a scan of the XMCD signal close to the L_3 absorption edge is shown for a different sample. A Gaussian fit to the XMCD data yields a FWHM of 0.47 eV and peak position at -0.2 eV with respect to the L_3 peak. Note that both features, the narrow

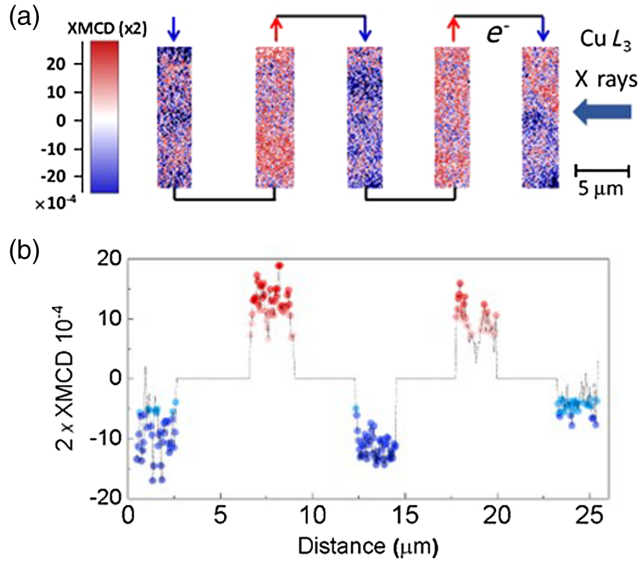


FIG. 3. (a) Visualization of the spin accumulation in a $\text{Cu}_{95}\text{Bi}_5$ electrode for sample S3. The graph shows the pixelwise up-down asymmetry of an XMCD image taken at the $\text{Cu } L_3$ edge, i.e., the subtraction of two areas with opposite current flow. Areas outside of the integration regions have been masked in order to improve clarity. (b) Horizontal profile through the data of (a), highlighting the alternating spin signal.

peak width (close to the minimum allowed due to the core hole lifetime) and the location before the XAS peak, are characteristic of spin accumulation at the Fermi edge [21].

In Fig. 3(a), we show a visualization of the spin accumulation in the $\text{Cu}_{95}\text{Bi}_5$ electrode by taking the pixelwise up-down asymmetry, i.e., the difference of the XMCD signal from the upper and lower part of each electrode branch, for one of the images acquired at the $\text{Cu } L_3$ edge. To improve the clarity, the areas outside the integration regions (i.e., outside the center of the electrodes) have been masked and the background flattened. The single XMCD image was taken from a run where the offset was small, and no prepeak subtraction was necessary. A clear *low-high-low-high-low* (blue-red-blue-red-blue) pattern in the five consecutive electrode branches can be observed, reflecting the alternating spin accumulation due to the alternating current direction. This oscillatory pattern is also visible in the profile of Fig. 3(b) which averages the data in Fig. 3(a) in the vertical direction. The full average over each area is the input of the fits which are used to quantify the XMCD signal (see Appendix F).

Figure 4 summarizes all the XMCD signals ($\text{Cu}_{95}\text{Bi}_5$ thickness between 20 and 50 nm, as indicated) where prepeak measurements were available to perform the offset subtraction. Datasets without prepeak normalization have been discarded, although some of them appeared reasonable (see, for example, Fig. 11), for the sake of consistency throughout the analysis. The thickness of all samples reported in Fig. 4 is well above the information depth,

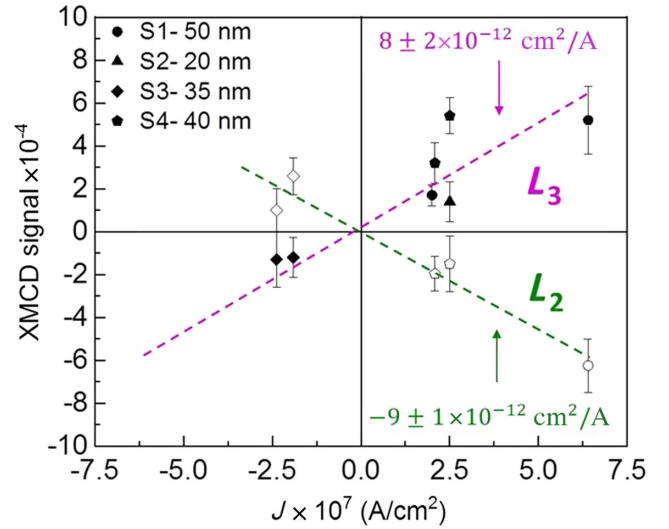


FIG. 4. XMCD signal as function of current density for measurements at the $\text{Cu } L_3$ and L_2 absorption peak energies, extracted as explained in the main text. Each point is an average of at least three measurements. The error bars correspond to the combined errors of peak and prepeak values. The dashed lines are linear fits to the data.

and thus the exclusive probing of the upper surface is guaranteed. Each data point is the average of at least three single measurements for each energy, peak and prepeak, respectively. The error bars represent the combined errors of the two photon energies. The data show a consistent sign inversion with respect to the injected current and the absorption peak (L_3 versus L_2). Dashed lines are linear fits to the data which yield XMCD coefficients of $(8 \pm 2) \times 10^{-12} \text{ cm}^2 \text{ A}^{-1}$ for the $\text{Cu } L_3$ and $(-9 \pm 1) \times 10^{-12} \text{ cm}^2 \text{ A}^{-1}$ for the $\text{Cu } L_2$.

Note that the absolute sign of the XMCD effect at the $\text{Cu } L_{3,2}$ absorption peaks due to spin polarization at the Fermi level should be the same as for the $3d$ magnetic metals such as Fe, because in both cases more empty *minority* final states are available for transitions. The measured sign is in agreement with a negative spin Hall angle in CuBi [15]; i.e., when the electron flow is upward in Figs. 1(b) and 1(c), a spin polarization parallel to the incident beam (blue arrow) is produced at the upper surface of the electrode.

The measured XMCD signals due to SHE at the $\text{Cu } L_3$ and L_2 , as given by the linear fits of Fig. 4, i.e., $(8 \pm 2) \times 10^{-12}$ and $(-9 \pm 1) \times 10^{-12} \text{ cm}^2 \text{ A}^{-1}$, are of opposite sign but almost equal strength. This relation is in agreement with Ref. [26], reporting XMCD spectra for a proximity-induced magnetization at the $\text{Cu } d$ shell for thin Cu layers sandwiched with Co , due to the hybridization between Co and $\text{Cu } d$ orbitals. The reason a comparison of that data with the SHE-induced spin polarization can be attempted is that even in the absence of Co , i.e., for pure bulk fcc Cu , the $L_{3,2}$ edges are probing almost exclusively $2p$ - $3d$ transitions, due to the $3d$ - $4s$ hybridization at the Fermi level and

very different transition matrix elements [27]. The induced magnetic moment is determined using the same procedure as the case of spin polarized current injection from a Co electrode, reported by Kukreja *et al.* [21] who also considered transitions into $3d$ states using Refs. [26,27]. The estimation is a lower bound because the XMCD values were measured at the XAS peak, located 0.2 eV above the peak of the XMCD spectrum. Using Ref. [26] and the width of a Gaussian XMCD peak profile in Fig. 2(b), 0.47 eV, the XMCD coefficient at the Cu L_3 translates to an induced magnetic moment of $(2.2 \pm 0.5) \times 10^{-12} \mu_B \text{ cm}^2 \text{ A}^{-1}$ per Cu atom as weighted average over the information depth (around 5 nm) [28]. For our typical current densities the average detected magnetic moment is thus approximately $5 \times 10^{-5} \mu_B/\text{atom}$.

Such a small value requires careful consideration of possible sources for spurious XMCD signals, which we discuss in the following. (a) The paramagnetic spin polarization due to the current-induced Oersted field is $< 1 \times 10^{-6} \mu_B/\text{atom}$ (see Appendix G), well below our signal level. (b) We can rule out sample imperfections since similar results were obtained on four different samples, and since slightly shifting the areas of integration did not significantly change the numbers. (c) Background variations in the XMCD images caused by the beam intensity distribution do not change with current polarity and could thus not be the origin of the consistent sign change for opposite current directions. (d) Background variations due to the local potential from the driving voltage, which could change sign with the current direction, are the reason why we do not directly compare images with opposite current but rather the upper and lower part of the electrode, which are joined by equipotential points (virtual ground) in the middle. In addition, the effect of the local potential does not depend on the photon energy and therefore it is eliminated by the subtraction of the offset from preedge energies. (e) Finally, any hypothetical artifact related to a combination of any of the previous with sample charging cannot explain the inversion of the signal between the L_3 and L_2 peaks.

The determined magnetic moment in $\text{Cu}_{95}\text{Bi}_5$, $(2.2 \pm 0.5) \times 10^{-12} \mu_B \text{ cm}^2 \text{ A}^{-1}$, is of the same order of magnitude as the values reported by Stamm *et al.* [8] for Pt detected by optical methods, i.e., $5 \times 10^{-12} \mu_B \text{ cm}^2 \text{ A}^{-1}$ for the topmost atomic layer (and $2 \times 10^{-12} \mu_B \text{ cm}^2 \text{ A}^{-1}$ for the upper half of the sample). In the cited work, the spin diffusion length was determined to be $\lambda_{sf}(\text{Pt}) = 11.4 \text{ nm}$ from the thickness dependence of the optical signal (Kerr rotation) and the SHA as $\alpha_{\text{Pt}} = 0.08$, for 300 K and $18\text{--}27 \mu\Omega \text{ cm}$ resistivity. The authors also give the expression which links the induced magnetic moment with the SHA, using the spin drift diffusion model of Zhang [29] within a Boltzmann transport equation framework. In order to calculate the spin Hall angle α for $\text{Cu}_{95}\text{Bi}_5$ from the measured magnetic moment, one needs the knowledge of

further material parameters (see Appendix H): the resistivity ρ , the Stoner enhancement factor F , the density of states at the Fermi level $D(\epsilon_F)$, and the spin diffusion length λ_{sf} . The resistivity ρ was determined experimentally as $13 \mu\Omega \text{ cm}$, whereas for F and $D(\epsilon_F)$ we use the Cu values as an estimation. We found some attenuation of the SHE signal for the thinnest sample (20 nm; see Fig. 4), but a single data point is not enough to obtain a reliable value for the spin diffusion length λ_{sf} . Instead, we present in Fig. 12 the SHA values corresponding to different values of λ_{sf} for $\text{Cu}_{95}\text{Bi}_5$. They have been computed taking into account the spin accumulation depth profile and the PEEM probing depth, as detailed in Appendix H. All our measurements, including the SHE signal attenuation for the thinnest sample, are compatible with a spin diffusion length in the 10–20 nm range and thus a SHA $|\alpha| \approx 0.20\text{--}0.25$. If the true spin diffusion length were shorter, the SHA would be even larger, with only a minor reduction for the opposite case (see Fig. 12). In comparison, Niimi *et al.* [15] report a SHA $\alpha_{\text{CuBi}} = -0.11$ and $\lambda_{sf} = 30\text{--}50 \text{ nm}$ for a CuBi alloy with lower doping (up to 0.5%) but similar resistivity, measured in nonlocal spin valves at 10 K, and an intrinsic limit for the skew scattering mechanism of -0.24 . These numbers are compatible with our measurements at 220 K, if the spin Hall angle in $\text{Cu}_{95}\text{Bi}_5$ is close to the intrinsic limit of Bi impurities in Cu. Our results thus indicate a larger spin Hall angle in $\text{Cu}_{95}\text{Bi}_5$ than previously reported for the CuBi alloy, approaching the efficiency of the skew scattering mechanism.

IV. CONCLUSION

In summary, using a photoemission electron microscope, we have detected a small XMCD signal at the Cu $L_{3,2}$ absorption edges from the surface of a CuBi electrode, through which an electrical current is flowing. The sign of this signal inverts with the sense of the injected current and is opposite for the L_3 and L_2 peaks. The size is similar at both peaks with $(8 \pm 2) \times 10^{-12}$ and $(-9 \pm 1) \times 10^{-12} \text{ cm}^2 \text{ A}^{-1}$, respectively. The XMCD peak shape and position are characteristic of spin accumulation at the Fermi level [21]. The spin accumulation at the $\text{Cu}_{95}\text{Bi}_5$ surface is ascribed to the spin Hall effect, reproducing the negative sign of the spin Hall angle of CuBi. The corresponding induced magnetic moment in $\text{Cu}_{95}\text{Bi}_5$ is $(2.2 \pm 0.5) \times 10^{-12} \mu_B \text{ cm}^2 \text{ A}^{-1}$ per Cu atom as weighted average over the information depth (about 5 nm). The results indicate a large spin Hall angle $\alpha \approx -0.20\text{--}0.25$ in $\text{Cu}_{95}\text{Bi}_5$, approaching the intrinsic limit of the skew scattering mechanism [15]. This large spin Hall efficiency reiterates the potential of CuBi for spin-charge conversion. Furthermore, our results constitute the proof of concept for the direct, interface-free and element-selective measurement of the SHE in a single material by means of x-ray spectromicroscopy.

ACKNOWLEDGMENTS

We thank Roopali Kukreja for answering our questions about Ref. [21] and Sergio O. Valenzuela and Olivier Fruchart for critical reading of the manuscript. We acknowledge M. R. Osorio and D. Granados at IMDEA-nanoscience nanofabrication center for their help in the lithography process. This work has been partially funded by MCIN/AEI/10.13039/501100011033 through Projects No. FIS2016-78591-C3-1-R, No. MAT2017-87072-C4-2-P, No. RTI2018-097895-B-C42, No. RTI2018-095303-B-C53, and No. PID2020-117024GB-C43 and by the Comunidad de Madrid through Project No. NANOMAGCOST-CM P2018/NMT-4321. IMDEA Nanociencia acknowledges support from the Severo Ochoa Programme for Centres of Excellence in R&D (Grants No. SEV-2016-0686 and No. CEX2020-001039-S). The work has been supported by the ALBA in-house research program. We thank the Spanish National Center of Electron Microscopy for Scanning Electron Microscopy measurements. M. W. K. acknowledges funding from Horizon 2020 Marie Skłodowska-Curie COFUND DOC-FAM, with Grant agreement No. 754397.

APPENDIX A: DETAILS OF *e*-BEAM LITHOGRAPHY

To define the structures, a bilayer of MMA 6% in ethyl lactate and of 950 kD (kiloDalton) molecular weight PMMA 4% in ethyl lactate was spin casted on top of the Si wafer. For both layers, the spin casting was performed at 3000 rpm for 60 sec, followed by a soft bake of the resist at 175 °C for 60 sec. The resist was then exposed at a dose of 1000 $\mu\text{C}/\text{cm}^2$ with a 100 keV electron beam using a Vistec EBPG 5000Plus electron beam writer. The exposed patterns were then developed by immersion in a solution of methyl-isobutyl-ketone 1:3 in isopropanol (volume) for 60 sec, followed by immersion in pure isopropanol for an additional 60 sec. The quality of the developed structures was verified by optical microscopy. Lift-off was performed by immersion in pure acetone.

APPENDIX B: Bi SEGREGATION AFTER EXCESSIVE CURRENT INJECTION AND JOULE HEATING EFFECTS

We have carefully checked any possible thermal effect in the measurements and there is no indication that Joule heating affects them. In any case, to avoid any contributions coming from changes in the temperature of the sample, all measurements were taken after 8–10 h of stabilization (i.e., with the sample cooled to 220 K and current applied to the electrodes—we used dc current in almost all reported measurements). Once the sample was stable, measurements were running during days without any evidence of sample damage, evolution of the signal with time, or any other aging effect. We only observed degradation of the samples for large current values, high enough to produce the

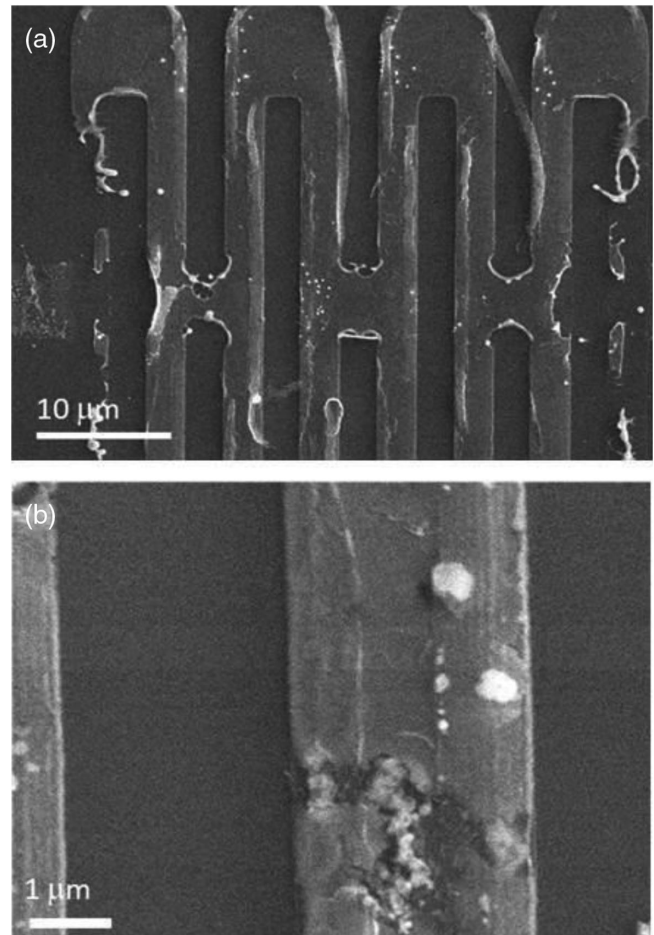


FIG. 5. Scanning electron microscopy images of a CuBi electrode structure after damage occurred by current injection of $8 \times 10^7 \text{ A}/\text{cm}^2$ at room temperature, exceeding the measurement conditions (maximum $5.4 \times 10^7 \text{ A}/\text{cm}^2$ at 220 K). The white dots were confirmed to be Bi rich.

segregation of Bi toward the surface, as we show in Fig. 5. Considering that Bi segregates above 90 °C, we can conclude that all measurements included in the analysis were performed below that temperature.

APPENDIX C: FINITE ELEMENT SIMULATION OF THE ELECTRIC AND MAGNETIC FIELD

Figure 6 shows a finite element simulation of a $\text{Cu}_{95}\text{Bi}_5$ electrode of 50 nm thickness and a simulated current density of $3.4 \times 10^6 \text{ A}/\text{cm}^2$ assuming a resistivity of $15 \mu\Omega \text{ cm}$. As shown in Fig. 6(a), the voltage drop along the structure resembles the color map obtained experimentally [Fig. 1(e)]. In the experiment, a voltage drop of about 2 V over 2 loops is observed for an applied current density of $1.7 \times 10^7 \text{ A}/\text{cm}^2$, while the simulations show 0.93 V over 4 loops. A comparison of these two values then yields a total resistivity of our sample of $13 \mu\Omega \text{ cm}$ at 220 K, which is expected to also include temperature-dependent (phonon) contributions. Note that in Ref. [15], for residual

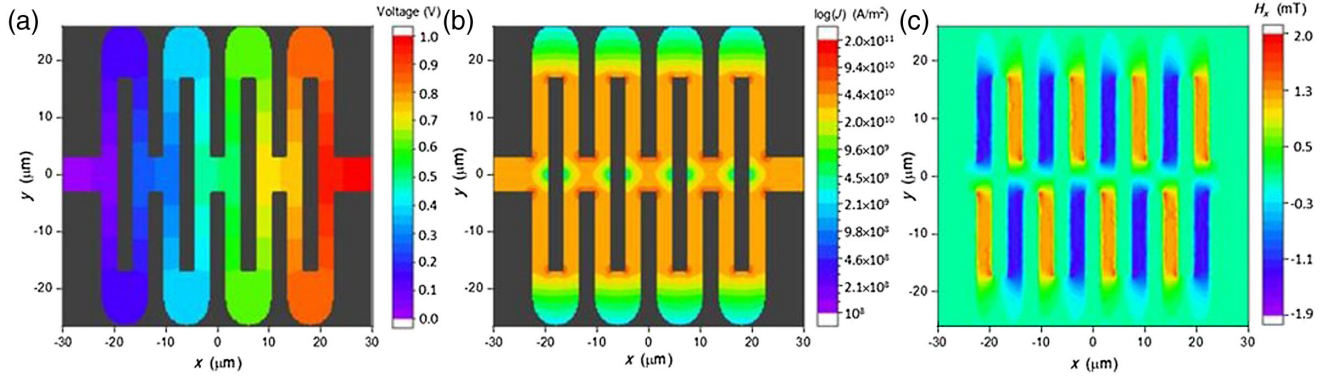


FIG. 6. Finite element simulation of the CuBi electrodes with current flow: (a) voltage drop along the structure, (b) current density along the structure in logarithmic scale, and (c) transverse magnetic field component.

resistivity contribution of the Bi impurities alone (i.e., after subtracting the Cu resistivity) of $3\text{--}5\ \mu\Omega\text{ cm}$ at 10 K, a large spin Hall angle is found.

Figure 6(b) shows that the magnitude of the current density in the straight vertical areas of the electrodes, which are used to extract the XMCD signal, is constant.

Figure 6(c) shows the transverse magnetic field component obtained in the upper surface of the electrode, which is about 1.2 mT. Considering the highest current density in our experiments of $j = 7 \times 10^7\ \text{A/cm}^2$, the maximum magnetic field at the surface is then around $B_x \approx 25\ \text{mT}$. As estimated in Appendix F, the induced paramagnetic moment due to this Oersted field is below $10^{-6}\ \mu_B/\text{atom}$, much smaller than the signal that we measure.

APPENDIX D: X-RAY PHOTOELECTRON SPECTRA OF OXIDIZED SAMPLES

Figure 7 shows the Bi $4f$ x-ray photoelectron spectra of a sample from which the capping layer has been removed by

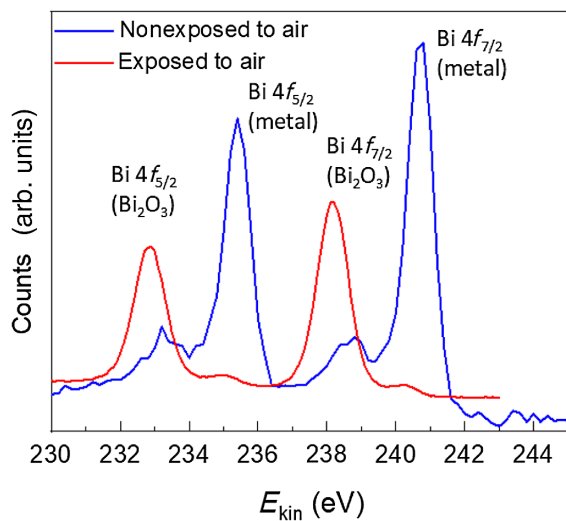


FIG. 7. Photoelectron spectrum of the Bi $4f$ core level of a sample after capping layer removal, before and after exposition to air.

Ar sputtering, before and after exposure to air. The spectrum before exposure shows mostly metallic Bi signal with a small oxide component while the sample exposed to air after the capping removal showed almost fully oxidized Bi.

APPENDIX E: XAS SPECTRA

Figure 8 shows the Cu L edge XAS spectra for all studied samples. In particular, the spectra in Fig. 2(b) were measured in sample S1 whereas the spectra of Fig. 10 were measured in sample S3. The difference between the spectra is just arising from the different sputtering times used for each sample before measuring, shorter in the latter. This may result in small differences in the remaining surface oxidation of the samples. From the spectra it is clear that the surface oxidation state is slightly different between samples. However, no correlation has been found between the SHE signal and the oxidation state within the experimental error.

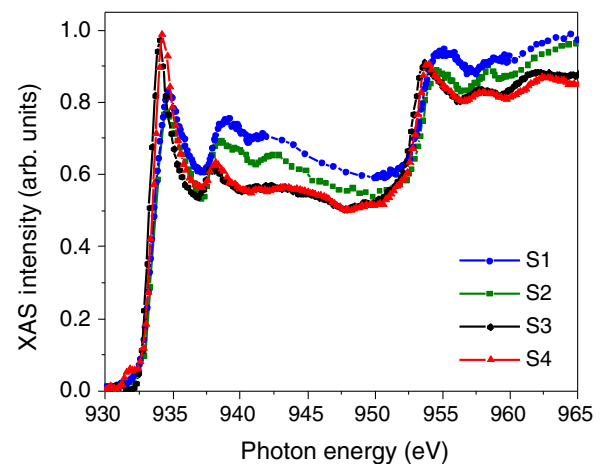


FIG. 8. Normalized x-ray absorption spectra of the Cu L edges for the samples measured in this work.

APPENDIX F: DATA TREATMENT

1. Fit process to obtain SHE raw signal

To extract the spin accumulation due to the SHE, the pixel averaged XMCD signal coming from each region marked with a yellow square in Fig. 9(a) was obtained from XMCD images as shown in Fig. 9(b). The contrast scale (black to white) in

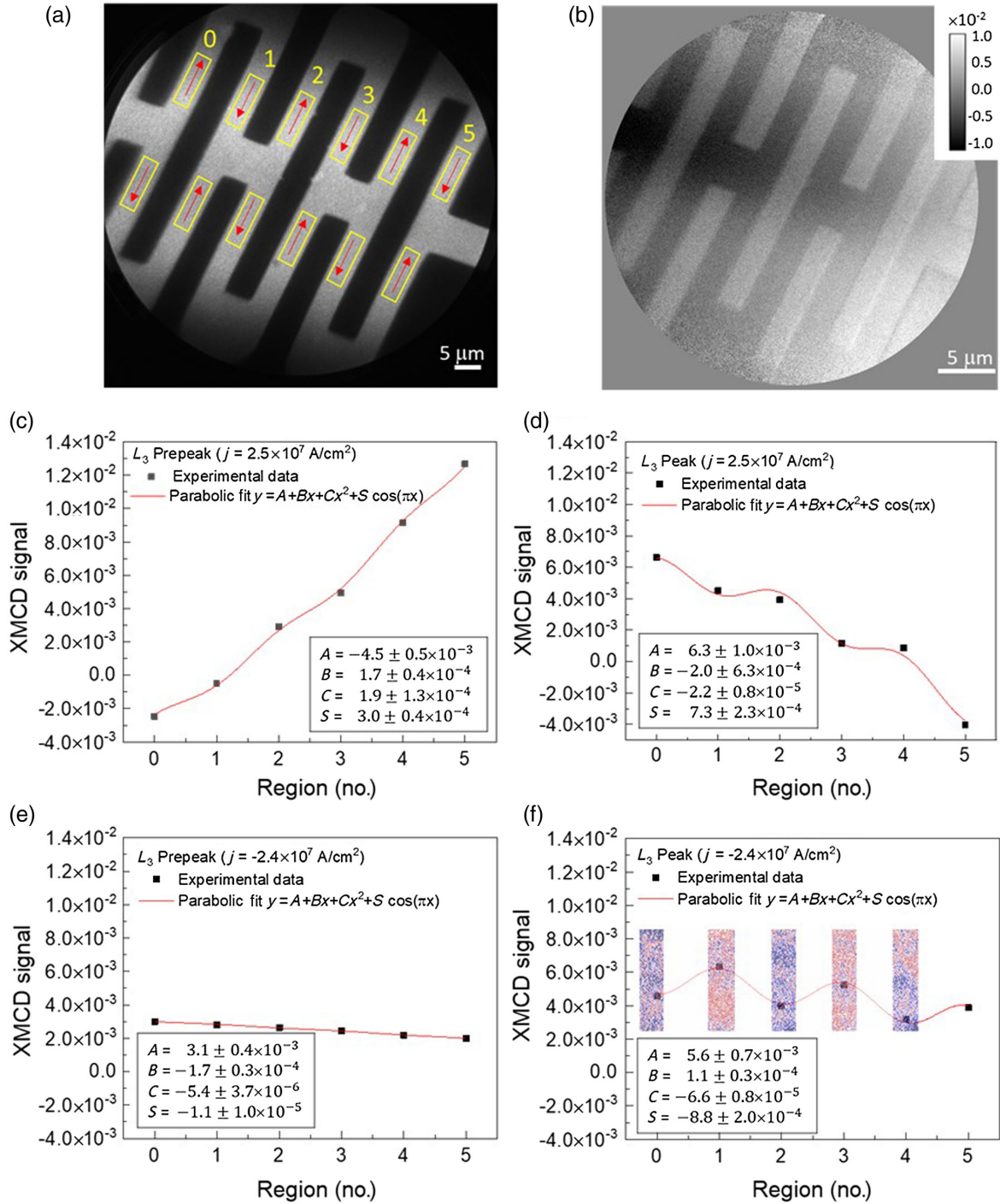


FIG. 9. (a) XAS image together with the regions (yellow squares) used to extract the XMCD signal. The red arrows show the direction of the current flow. (b) Example of an XMCD image at the L_3 peak photon energy for samples S3 and S4. (c)–(f) Examples of XMCD values as difference of the upper and lower area versus branch number of the electrode for the L_3 prepeak and L_3 peak photon energy. A parabolic fit (inset) is used to compensate the background and extract the alternating SHE contribution S^* . We have chosen a pair of examples with very low and very high background variation.

Fig. 9(b) is rather large, around 2.1%, because it needs to accommodate the background. The insulating silicon oxide surface appears in a different shade due to charging effects. In order to reduce the background contribution coming from the voltage drop along the structure and the difference between the beam intensity for the two polarizations, each single XMCD value indicated as a data point in Figs. 9(c)–9(f) is the difference (asymmetry) of the signal from two vertically aligned regions with the same potential but opposite currents, e.g., labeled 1a and 1b in panel of Fig. 1(c).

As can be seen in Figs. 9(c)–9(f), where the signal is plotted versus the position (electrode branch number), the background is then strongly reduced but still present. The signal of the spin Hall effect is a small alternating signal on top of the background. To determine it, a parabolic fit (see inset) including an oscillating term S was performed for all the measurements. The fit parameter S is then twice the XMCD signal coming from the spin accumulation due to the spin Hall effect in a single area. For Figs. 9(c)–9(f), we have selected on purpose examples with little and large background variations. As expected, even for the data with a strong background present, the S value is smaller [almost negligible in Fig. 9(e)] for off-peak energies.

2. Prepeak subtraction

Plotting the value of the S fit parameter ($S/2$ in Fig. 10) as a function of the energy, one sees that the XMCD signal has opposite values in L_3 and L_2 edges. However, even for off-peak energies where no XMCD signal is expected, an offset is typically found. As can be seen in Fig. 10, this offset can be different for the different measurement series. For example, while raw data at the L_2 peak are very similar for opposite current directions, there is a clear opposite signal when comparing values at L_2 with the corresponding

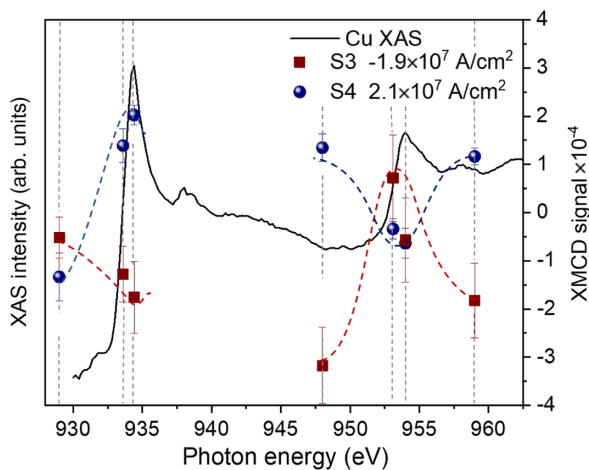


FIG. 10. X-ray absorption spectrum of the Cu L edge together with the value of the XMCD signal obtained at different energies as the average of at least three measurements. Dashed lines are guide to the eye.

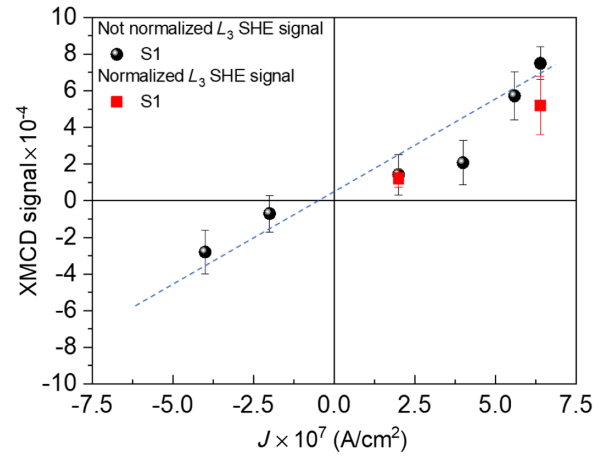


FIG. 11. Comparison of XMCD values at the L_3 peak for a single sample, with and without offset subtraction (illustrating a case where not all prepeak measurements were measured). Black symbols denote data without subtraction of the prepeak offset, red symbols with the offset subtracted. The dashed line is the same as in Fig. 3(c). Data measured in sample S1.

prepeak and after peak measurements. The offset was found to vary little over time and photon energy within a given dataset, recorded at constant current and within several hours. Therefore, a normalization of the XMCD signal for the L_3 and L_2 peaks as the difference of the value obtained at the absorption peak and the value obtained by an immediately preceding measurement at a prepeak photon energy was performed. The analysis of all data where this method was applicable, from four different samples and different measurement campaigns, is fully consistent and shown in Fig. 4.

In Fig. 11, we show an example to assess the influence of the prepeak subtraction. Black symbols represent values obtained directly for a single photon energy (L_3 peak), averaged over several images. However, only for two current densities the prepeak measurement is available (red symbols, after subtraction) and only those were included in Fig. 3(c). The dashed line is the same linear fit to the data as in Fig. 3(c) and it also describes these measurements reasonably. Although in this case the influence of the offset is only moderate, we included only those measurements into the final analysis where the offset correction could be performed.

APPENDIX G: PARAMAGNETIC MOMENT FROM OERSTED FIELD

One needs to consider the effect of the current-induced Oersted field, which also produces a small paramagnetic spin polarization at the sample surface: using $m = \mu_B^2 D(E_F) \mu_0 H$ [30], where $D(E_F)$ is the density of states at the Fermi energy (taking around 0.55 eV^{-1} per atom [31]), the expected moment for Cu would be $m = 3.2 \times 10^{-5} \mu_B \text{ T}^{-1}$ per atom. Following Ref. [32] we estimate the

transverse magnetic field component at the top surface as $B_x = \mu_0 j z$, where j is the current density and z the vertical distance from the stripe center. The highest value in our experiments is thus (for $j = 7 \times 10^7 \text{ A cm}^{-2}$ and $z = 25 \text{ nm}$) $B_x \approx 22 \text{ mT}$ (in agreement with the simulated value 25 mT in Appendix C). Therefore, the paramagnetic moment resulting from the Oersted field (below $10^{-6} \mu_B/\text{atom}$) is much smaller than the signal that we measure.

APPENDIX H: ANALYSIS OF THE MAGNETIC MOMENT

According to Stamm *et al.* [8] [combining Eqs. (S5) and (S6)], based on the work of Zhang [29], the spin accumulation per current density j , at depth z , is given by

$$M_j(z) = \frac{M_y(z)}{j} = \lambda_{\text{sf}} \alpha \rho \frac{\sinh(\frac{t-2z}{2\lambda_{\text{sf}}})}{\cosh(\frac{t}{2\lambda_{\text{sf}}})} D(\epsilon_f) F, \quad (\text{H1})$$

in units of μ_B per atom. Here, t is the sample thickness, λ_{sf} is the spin diffusion length, α is the spin Hall angle, ρ the resistivity, $D(\epsilon_f)$ is the total density of states at the Fermi level, and F is the Stoner enhancement factor. This expression is valid for λ_{sf} reasonably smaller than t , and thus as will be seen later, for the parameter range for which we can make some statement.

The PEEM depth-dependent sensitivity is modeled by the following function:

$$H(z) = e^{-(z/d)}, \quad (\text{H2})$$

with $d = 2 \text{ nm}$ [23].

The PEEM detected moment per atom and unit of current density is then

$$m_j(t) = \int_0^t dz M_j(z) H(z) / \int_0^t dz H(z). \quad (\text{H3})$$

Solving the integrals and substituting values for ρ , $D(\epsilon_f)$, and F , we obtain an expression for α as function of λ_{sf} and the sample thickness t in nanometers:

$$8.0366 \times 10^{-8} \alpha \lambda_{\text{sf}}^2 \frac{e^{-t/2\lambda_{\text{sf}}}}{2 \cosh(\frac{t}{2\lambda_{\text{sf}}}) (e^{t/d} - 1)} \times \left[\frac{e^{t[(1/\lambda_{\text{sf}})+(1/d)]} - 1}{\lambda_{\text{sf}} + d} + \frac{e^{t/\lambda_{\text{sf}}} - e^{t/d}}{\lambda_{\text{sf}} - d} \right] = 2.2 \times 10^{-12}. \quad (\text{H4})$$

The prefactors used are $D(\epsilon_f) = 0.55 \text{ eV}^{-1}$ per atom [32], and the Stoner enhancement factor F is given by

$$F = \frac{1}{1 - \ln(\epsilon_f)} = 1.124, \quad (\text{H5})$$

Since $\ln(\epsilon_f) = 0.11$ according to Ref. [33]. The values for these two parameters are thus taken for Cu as an approximation. A more precise determination of these parameters for $\text{Cu}_{95}\text{Bi}_5$ is beyond the scope of this work, which is

primarily dedicated to the demonstration of a measurement of the SHE with x-ray spectroscopy, but it remains interesting for the future. The experimental resistivity of the samples is $13 \mu\Omega \text{ cm}$. Equation (H4) yields a function $\alpha(\lambda_{\text{sf}})$ based on the determined magnetic moment from XMCD PEEM. It further depends on the sample thickness t , as the spin accumulation is reduced when the thickness is comparable to the spin diffusion length λ_{sf} . Since there is no direct information on the spin diffusion length λ_{sf} from our data, the equation is to be understood as follows: if the real spin diffusion length was λ_{sf} , then the spin Hall angle which corresponds to the magnetic moment would be α .

Figure 12 shows as solid lines the curves for the same magnetic moment and three characteristic thicknesses in our study, namely, 20, 35, and 50 nm. The curves for the 35- and 50-nm-thick samples indicate a lower bound of the SHA $|\alpha| \approx 0.20$ for long spin diffusion length λ_{sf} around or above 20 nm; those values are compatible with the results of Niimi *et al.* [15]. However, if the real value of λ_{sf} is lower, then the absolute value of the SHA $|\alpha|$ needs to be higher in order to still be compatible with the measured magnetic moment. However, the single data point available for the 20-nm-thick sample indicates a lower induced XMCD signal, possibly reduced by up to 50% (see Fig. 4). A good agreement between the 20 nm thin and the thicker samples is found when comparing the dashed curve in Fig. 11, which corresponds to a reduced magnetic moment (for the 20 nm sample) of $(1.1 \pm 0.5) \times 10^{-12} \mu_B \text{ cm}^2 \text{ A}^{-1}$. All measurements are compatible with

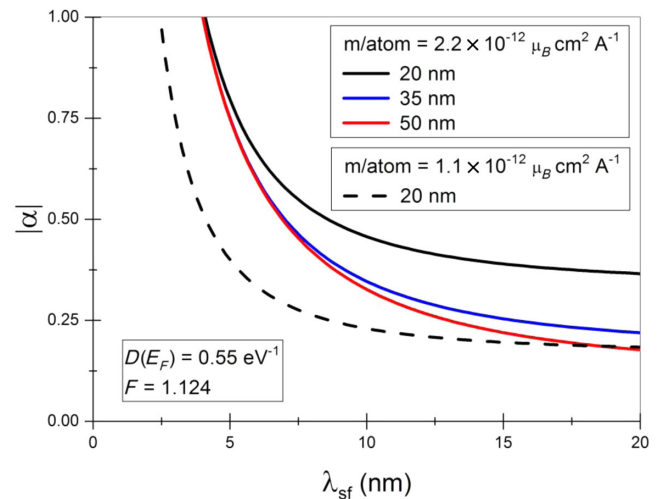


FIG. 12. Calculated relation of the spin diffusion length and the spin Hall angle in $\text{Cu}_{95}\text{Bi}_5$ for the magnetic moment measured by XMCD PEEM (linear fit in Fig. 4). Further calculation parameters are the measured resistivity and the density of states at Fermi level and Stoner factor taken for Cu. Curves of equal magnetic moment are plotted for different sample thickness. For the thinnest sample (20 nm) two curves are calculated, one for the full magnetic moment and one for a reduced magnetic moment to one-half.

a spin diffusion length in the 10–20 nm range and a SHA $|\alpha| \approx 0.20\text{--}0.25$. It should be noted that this treatment is at the limit of the applicability of the spin drift diffusion model (t could be comparable to λ_{sf}); clearly, further experiments are needed to gain more insight into the SHA of Cu_9Bi_5 .

- [1] J. E. Hirsch *Spin Hall Effect*, *Phys. Rev. Lett.* **83**, 1834 (1999).
- [2] M. I. Dyakonov and V. I. Perel, *Current-Induced Spin Orientation of Electrons in Semiconductors*, *Phys. Lett. A* **35**, 459 (1971).
- [3] N. F. Mott, *The Scattering of Fast Electrons by Atomic Nuclei*, *Proc. R. Soc. A* **124**, 425 (1929).
- [4] J. Sinova, S. O. Valenzuela, J. Wunderlich, C. H. Back, and T. Jungwirth, *Spin Hall Effects*, *Rev. Mod. Phys.* **87**, 1213 (2015).
- [5] A. Hoffman, *Spin Hall Effects in Metals*, *IEEE Trans. Magn.* **49**, 5172 (2013).
- [6] Y. K. Kato, R. C. Myers, A. C. Gossard, and D. D. Awschalom, *Observation of the Spin Hall Effect in Semiconductors*, *Science* **306**, 1910 (2004).
- [7] J. Wunderlich B., Kaestner J., and Sinova T. Jungwirth, *Experimental Observation of the Spin-Hall Effect in a Two-Dimensional Spin-Orbit Coupled Semiconductor System*, *Phys. Rev. Lett.* **94**, 047204 (2005).
- [8] C. Stamm, C. Murer, M. Berritta, J. Feng, M. Gabureac, P. M. Oppeneer, and P. Gambardella, *Magneto-Optical Detection of the Spin Hall Effect in Pt and W Thin Films*, *Phys. Rev. Lett.* **119**, 087203 (2017).
- [9] M. Baumgartner, K. Garello, J. Mendil, C. O. Avci, E. Grimaldi, C. Murer, J. Feng, M. Gabureac, C. Stamm, Y. Acremann, S. Finizio, S. Wintz, J. Raabe, and P. Gambardella, *Spatially and Time-Resolved Magnetization Dynamics Driven by Spin-Orbit Torques*, *Nat. Nanotechnol.* **12**, 980 (2017).
- [10] S. Finizio, S. Wintz, S. Mayr, A. J. Huxtable, M. Langer, J. Bailey, G. Burnell, C. H. Marrows, and J. Raabe, *Time-Resolved Visualization of the Magnetization Canting Induced by Field-like Spin-Orbit Torques*, *Appl. Phys. Lett.* **117**, 212404 (2020).
- [11] M. Martins and W. Wurth, *Magnetic Properties of Supported Metal Atoms and Clusters*, *J. Phys. Condens. Matter* **28**, 503002 (2016).
- [12] M. Ormaza, L. Fernández, M. Ilyn, A. Magaña, B. Xu, M. J. Verstraete, M. Gastaldo, M. A. Valbuena, P. Gargiani, A. Mugarza, A. Ayuela, L. Vitali, M. Blanco-Rey, F. Schiller, and J. E. Ortega, *High Temperature Ferromagnetism in a GdAg_2 Monolayer*, *Nano Lett.* **16**, 4230 (2016).
- [13] P. Gambardella, S. Rusponi, M. Veronese, S. S. Dhesi, C. Grazioli, A. Dallmeyer, I. Cabria, R. Zeller, P. H. Dederichs, K. Kern, C. Carbone, and H. Brune, *Giant Magnetic Anisotropy of Single Cobalt Atoms and Nanoparticles*, *Science* **300**, 1130 (2003).
- [14] C. Stamm, C. Murer, Y. Acremann, M. Baumgartner, R. Gort, S. Däster, A. Kleibert, K. Garello, J. Feng, M. Gabureac, Z. Chen, J. Stöhr, and P. Gambardella, *X-Ray Spectroscopy of Current-Induced Spin-Orbit Torques and Spin Accumulation in Pt/3d-Transition-Metal Bilayers*, *Phys. Rev. B* **100**, 024426 (2019).
- [15] Y. Niimi, Y. Kawanishi, D. H. Wei, C. Deranlot, H. X. Yang, M. Chshiev, T. Valet, A. Fert, and Y. Otani, *Giant Spin Hall Effect Induced by Skew Scattering from Bismuth Impurities inside Thin Film CuBi Alloys*, *Phys. Rev. Lett.* **109**, 156602 (2012).
- [16] Y. Wang, P. Deorani, X. Qiu, J. H. Kwon, and H. Yang, *Determination of Intrinsic Spin Hall Angle in Pt*, *Appl. Phys. Lett.* **105**, 152412 (2014).
- [17] Larger values for Pt (up to a bulk SHA $\alpha = 0.387$) have been reported in A. J. Berger, E. R. J. Edwards, H. T. Nembach, O. Karis, M. Weiler, and T. J. Silva, *Determination of the Spin Hall Effect and the Spin Diffusion Length of Pt from Self-Consistent Fitting of Damping Enhancement and Inverse Spin-Orbit Torque Measurements*, *Phys. Rev. B* **98**, 024402 (2018).
- [18] S. Ruiz-Gomez, A. Serrano, R. Guerrero, M. Munoz, I. Lucas, M. Foerster, L. Aballe, J. F. Marco, M. Amado, L. McKenzie-Sell, A. di Bernardo, J. W. A. Robinson, M. A. Gonzalez Barrio, A. Mascaraque, and L. Perez, *Highly Bi-Doped Cu Thin Films with Large Spin-Mixing Conductance*, *Appl. Phys. Lett. Mater.* **6**, 101107 (2018).
- [19] H. Wang, C. Du, P. C. Hammel, and F. Yang, *Comparative Determination of $\text{Y}_3\text{Fe}_5\text{O}_{12}/\text{Pt}$ Interfacial Spin Mixing Conductance by Spin-Hall Magnetoresistance and Spin Pumping*, *Appl. Phys. Lett.* **110**, 062402 (2017).
- [20] A. Brataas, G. E. W. Bauer, and P. J. Kelly, *Non-Collinear Magnetoelectronics*, *Phys. Rep.* **427**, 157 (2006).
- [21] R. Kukreja, S. Bonetti, Z. Chen, D. Backes, Y. Acremann, J. A. Katine, A. D. Kent, H. A. Dürr, H. Ohldag, and J. Stöhr, *X-Ray Detection of Transient Magnetic Moments Induced by a Spin Current in Cu*, *Phys. Rev. Lett.* **115**, 096601 (2015).
- [22] J. Ding, W. Zhang, M. B. Jungfleisch, J. E. Pearson, H. Ohldag, V. Novosad, and A. Hoffmann, *Direct Observation of Spin Accumulation in Cu Induced by Spin Pumping*, *Phys. Research* **2**, 013262 (2020).
- [23] B. H. Frazer, B. Gilbert, B. R. Sonderegger, and G. de Stasio, *The Probing Depth of Total Electron Yield in the Sub-keV Range: TEY-XAS and X-PEEM*, *Surf. Sci.* **537**, 161 (2003).
- [24] L. Aballe, M. Foerster, E. Pellegrin, J. Nicolas, and S. Ferrer, *The ALBA Spectroscopic LEEM-PEEM Experimental Station: Layout and Performance*, *J. Synchrotron Radiat.* **22**, 745 (2015).
- [25] M. Foerster, J. Prat, V. Massana, N. Gonzalez, A. Fontseré, B. Molas, O. Matilla, E. Pellegrin, and L. Aballe, *Custom Sample Environments at the ALBA XPEEM*, *Ultramicroscopy* **171**, 63 (2016).
- [26] M. G. Samant, J. Stöhr, S. S. P. Parkin, G. A. Held, B. D. Hermsmeier, F. Herman, M. Van Schilfgaarde, L.-C. Duda, D. C. Mancini, N. Wassdahl, and R. Nakajima, *Induced Spin Polarization in Cu Spacer Layers in Co/Cu Multilayers*, *Phys. Rev. Lett.* **72**, 1112 (1994).
- [27] H. Ebert, J. Stöhr, S. S. P. Parkin, M. Samant, and A. Nilsson, *L-Edge X-Ray Absorption in fcc and bcc Cu Metal: Comparison of Experimental and First-Principles Theoretical Results*, *Phys. Rev. B* **53**, 16067 (1996).

- [28] The conversion from XMCD to magnetic moment uses Eqs. (1) and (2) of Ref. [26], assuming a negligible orbital moment to obtain $m = 3\Delta A_{L_3}/C^*$ with the proportionality constant $C^* = -5.6 \text{ eV } \mu_B^{-1}$ (the unit eV is not explicitly mentioned in Ref. [26]). The XMCD area ΔA_{L_3} is calculated for a Gaussian peak with $8 \times 10^{-12} \text{ cm}^2 \text{ A}^{-1}$ height and 0.47 eV width.
- [29] S. Zhang, *Spin Hall Effect in the Presence of Spin Diffusion*, *Phys. Rev. Lett.* **85**, 393 (2000).
- [30] N. W. Ashcroft and N. D. Mermin, *Solid State Physics* (Harcourt College publishers, Orlando, FL, 1976).
- [31] O. Bunău and Y. Joly, *Self-Consistent Aspects of X-Ray Absorption Calculations*, *J. Phys. Condens. Matter* **21**, 345501 (2009).
- [32] V. Uhlíř, S. Pizzini, N. Rougemaille, V. Cros, E. Jiménez, L. Ranno, O. Fruchart, M. Urbánek, G. Gaudin, J. Camarero, C. Tieg, F. Sirotti, E. Wagner, and J. Vogel, *Direct Observation of Oersted-Field-Induced Magnetization Dynamics in Magnetic Nanostripes*, *Phys. Rev. B* **83**, 020406 (2011).
- [33] J. F. Janak, *Uniform Susceptibilities of Metallic Elements*, *Phys. Rev. B* **16**, 255 (1977).